Title
Heat Spreader Design for Improved Performance and Reliability of II-V Quantum Dot Lasers

Author
Collins, Noelle

Publication Date
2020

Peer reviewed|Thesis/dissertation

UNIVERSITY OF CALIFORNIA

Santa Barbara

Heat Spreader Design for Improved Performance and Reliability of II-V Quantum Dot Lasers

A Thesis submitted in partial satisfaction of the

requirements for the degree Master of Science

in Electrical and Computer Engineering

by

Noelle M. Collins

Committee in charge:

Professor John Bowers, Chair

Professor Daniel Blumenthal

Professor Clint Schow

September 2020

The thesis of Noelle Collins is approved.

Clint Schow

Daniel Blumenthal

John Bowers, Committee Chair

June 2020

ABSTRACT

Heat Spreader Design for Improved Performance and Reliability of III-IV Quantum Dot Lasers

by

Noelle Collins

We designed heat spreaders to efficiently transfer heat from a III-V epitaxially grown quantum dot laser to a heat sink. This will efficiently remove excess heat and improve many aspects of the laser's performance including increased output power, improved slope efficiency, decreased threshold current, better wavelength stability, and extended device lifetime. For this project, we simulated the thermal impedance of the laser with an attached diamond or AlN heat spreader using COMSOL. We also designed laser and heat spreader masks and designed a fabrication process for the lasers. In future work, we will manufacture the lasers, flip chip bond them to the heat spreaders, and characterize their performance and reliability.

I. Introduction

Power management is crucial to datacenter operation, as datacenters consume huge amounts of power. In 2020, datacenters are projected to consume 73 billion kWh in the United States [1]. Datacenters can improve efficiency and bandwidth by using optical interconnects instead of electrical interconnects. The need to improve efficiency in datacenters drives innovation in laser diodes and likewise in efficient heat management of these devices, which improves laser performance. As bandwidth needs in datacenters inevitably increase innovations in thermal management will be imperative. The proposed heat spreader in this thesis is a viable option to meet this demand.

The thermal properties of a diode laser are inextricably linked to its performance and lifetime. This is especially true for high-powered lasers where excess heat is particularly problematic irrespective of wall-plug efficiency. Efficient removal of excess heat has many benefits: increased output power, reduced threshold current, improved slope efficiency, better wavelength stability, and extended device lifetime. More precisely, a diode laser's output power is limited by thermal rollover [2]. The threshold current of a laser increases exponentially with increasing junction temperature, while slope efficiency decreases exponentially with increasing junction temperature [2][3]. Moreover, the lasing wavelength shifts with changes in junction temperature, and many studies show that operating lifetime decreases exponentially with increasing temperature [3][4]. Therefore, thermal management of diode lasers is critically important. In this thesis, we propose thermal management of an InAs quantum dot Fabry-Perot laser diode epitaxially grown on silicon using heat spreaders made from materials with high thermal conductivities.

The laser used in this thesis is grown on silicon. Silicon photonics is burgeoning field, which has driven innovation in silicon-based lasers. Despite the challenges laser integration on silicon presents due to its indirect bandgap, a few viable options for integrated lasers on silicon emerged in the past couple of decades. The laser described in this thesis is based on III-V materials epitaxially grown directly on silicon [5]. Other forms of integrated lasers on silicon instead use native III-V wafers bonded onto silicon. This method has shown remarkable device performance but is less scalable and more expensive than the laser used here [5]. III-V devices directly grown on silicon are more scalable and less expensive, which are both important considerations for datacenter applications [5].

Without the use of a high thermal conductivity heat spreader, the silicon substrate that the laser is grown on essentially acts as a heat spreader; heat flows from the laser junction down through the silicon substrate to a thermal electric cooler (TEC), which acts as a heat sink. Packaging this laser with the heat spreader proposed in this thesis cools the junction more efficiently because it is made from AlN or Diamond, which both have higher thermal conductivity than silicon. The heat spreader also cools the laser junction by adding an additional path for heat to dissipate. Furthermore, the heat spreader's compact and simple design is suitable for data center environments where device and packaging footprint as well as cost are major considerations [6].

A. Junction Temperature and Thermal Impedance Background Information

As stated earlier, efficient removal of excess heat from the junction has many benefits: increased output power, reduced threshold current, improved slope efficiency, better wavelength stability, and extended device lifetime. Therefore, it is important to understand which factors influence the junction temperature in order to formulate an effective plan to minimize it. We start by defining the junction temperature (T_j) [7][8]

$$T_j = T_{hs} + \Delta T \qquad (1)$$

T_{hs} is the temperature of the heat sink. In our case, the heat sink is a TEC, which we set to a constant temperature. We define ΔT as the difference between the active region temperature and the ambient temperature. Additionally, ΔT is approximately equal to

$$\Delta T = Zth*P_D \qquad (2)$$

Z_{th} is the thermal impedance of the laser, and P_D is the dissipated power in the laser. Specifically, P_D is the difference between the electrical input power and the optical output power defined in (4). We define the conversion or wall-plug efficiency (η) in equation (3), which measures the optical power out (P_{out}) relative to the electrical input power (P_{in}) [7]

$$\eta = P_{out}/P_{in} \qquad (3)$$

Also,

$$P_D = P_{in} - P_{out} \qquad (4)$$

Substituting equations (1) - (4) we get

$$T_j = T_{hs} + Z_{th}*P_{in}*(1-\eta) \qquad (5)$$

From this equation, several strategies to reduce junction temperature emerge [8]. Clearly, we can reduce the input power to lower the junction temperature; however, since our goal is to maximize the output power of the laser this option is not ideal. Our first viable option is to increase the wall-plug efficiency of the laser. Secondly, we can reduce the heat sink temperature. Finally, we can reduce the laser’s thermal impedance, which is the focus of this work. The thermal impedance of a diode laser describes how easily the laser dissipates heat and is measured in °C/W. The less the laser heats up for a given input power, the lower the thermal impedance. This thesis focuses on effectively packaging a diode laser to reduce its thermal impedance.

B. *Packaging: Basic Background Information*

In this thesis we thermally manage a laser through packaging it. Therefore, we must first understand a basic laser package. The simplest configuration consists of a laser bar soldered p-side down onto a heat sink (Figure 1) [8]. This type of package relies on conduction cooling [8]. The red arrows in Figure 1 show the path of heat from the hotter laser junction to the cooler heat sink.

If passive conduction cooling is inadequate, liquid cooling systems can be added to aid heat removal. Liquid cooling is often more costly and complicated and is often not necessary for packages like the one proposed in this paper that consist of a single emitter. For this reason, liquid cooling will not be discussed in further detail though these references explore the topic further [8][9].

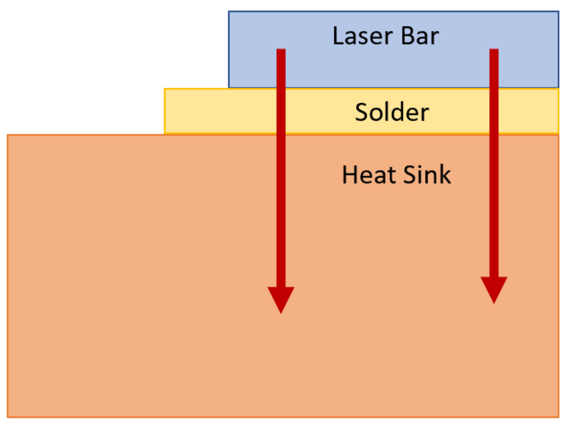

Figure 1. Simplified laser package with laser bar, solder, and heat sink. The arrows show the path of heat from the hotter laser bar to the cooler heat sink.

In a typical GaAs laser package, the laser is soldered p-side down, so that the contact pad below the laser is the p-contact, and the n-contact is formed on top of the laser through the GaAs substrate [8]. In our lasers, the silicon substrate presents a unique packaging challenge because n contact cannot be formed through the substrate. Therefore, we must form both an n and p contact below the laser. This design constraint adds additional challenges for flip chip bonding the laser onto the heat spreader. This process must be done more precisely than the traditional p-side down method, leaving little room for error. This constraint also limits the types of soldering materials appropriate for this application. Background on packaging materials as well as justification for our chosen materials is delineated in the next section.

C. Packaging Materials and Tradeoffs Overview

The tradeoff between thermal conductivity and the thermal expansion coefficient is an important consideration in laser packaging. The coefficient of thermal expansion (CTE) measures the change in size of a material per degree in temperature at a constant pressure. As a laser operates it changes temperature and changes size, expanding and contracting. This also happens to the materials around the laser, which comprise the laser package. Since each material has a unique coefficient of thermal expansion they will expand and contract different amounts for a given temperature change. This CTE mismatch can add excess strain in the package, which can lead to premature device failure. To accommodate for this, engineers often choose packaging materials with similar CTEs. A common combination is to package a GaAs laser with an AlN heat spreader; their CTEs are relatively well matched at 5.4 (pmm/K) and 4.5 (pmm/K), respectively (see Table 1). Another approach is to use a "soft" solder like indium, which alleviates stress between materials with dissimilar CTEs because of its high ductility.

Even with these techniques, it is insufficient to solely consider CTE when choosing packaging materials. The other important material consideration for packaging is thermal conductivity, which describes a material's ability to transfer heat. A material with a high thermal conductivity will transfer heat more quickly than material with a lower thermal conductivity and perform better as a heat spreader. When a material with a high thermal conductivity is used as a heat spreader for a diode laser, it lowers the laser's thermal impedance and allows it to quickly dissipate heat from the junction. Clearly, the ideal packaging material will maximize thermal conductivity without adding excessive strain in the laser package from an incompatible CTE [10].

A common example of this tradeoff in industry is a GaAs laser packaged on a copper heat sink with indium solder. Copper is an ideal heat sink choice because it is inexpensive and has a high thermal conductivity of 385 (W/mK). However, copper has a CTE of around 16.5 (pmm/K), while a typical laser made of GaAs has a CTE of around 5.4(pmm/K). To accommodate for the CTE mismatch, indium is typically used as solder. Although indium helps alleviate the CTE mismatch problem, it also presents challenges. Indium is considered a "soft" solder material and has a low melting point (156.6 ºC), which makes it an unsuitable solder choice for applications that require a heat sink temperature above 50 ºC. Additionally, indium's ductility makes soldering with precision difficult. Alternatively, GaAs lasers are packaged with an AlN heat spreader, which has a better matched CTE and does not require indium solder.

Our design requires precision soldering, so we chose a "hard" solder (AuSn) over indium. Additionally, as datacenters use a massive amount of power, they can be very hot environments; for this reason, indium may not be an appropriate solder choice. We chose AlN and diamond for our heat spreader material. Diamond is an ideal choice because it has the highest thermal conductivity of any material. The chemical vapor deposition (CVD) diamond we purchased has a CTE of 1800 (W/mK), which offers an order of magnitude improvement compared to the thermal conductivity of silicon (Table 1). Although the CTE of diamond is small, the CTE mismatch is not as severe in our lasers, which have a silicon substrate as opposed to a typical laser grown on a native GaAs substrate (Table 1). We also chose an identical AlN heat spreader to determine which heat spreader material leads to better device lifetimes. We can do this by aging identical lasers soldered on otherwise identical heat spreaders made of these different materials. Finally, although the focus of this thesis is on heat spreaders for InAs QD lasers grown on silicon we also want to package and test lasers on native substrates. For this application, AlN is an obvious heat spreader material choice.

Material	**CTE (pmm/K)**	**Thermal Conductivity (W/mK)**
GaAs	5.4	46
Si	2.6	150
Diamond	1	1800
AlN	4.5	200
AuSn	16	57
Cu	16.5	385

Table 1. CTE and thermal conductivities of common packaging materials

D. Quantum Dot Laser Overview

Most simply, a diode laser consists of a forward biased P-N diode, with the active medium acting as the junction of the diode. In our case, the active medium consists of InAs quantum dots. Current is injected into the active region via the N and P type layers. Light is confined in the active region because it has a higher refractive index than the surrounding cladding layers. Once a minimum current density is reached, known as the threshold current, the laser will lase. Additional current beyond threshold will increase the laser's output power.

To grow this laser, a GaAs buffer is first is grown on top of the silicon wafer, followed by the n GaAs and n AlGaAs layers. Next, the active region with the InAs quantum dots is grown, and finally the p AlGaAs and p GaAs p layers are grown. Once all the epitaxial layers are grown the laser is fabricated as shown in Figure 2, which shows a simplified cross-sectional representation of the laser with light blue SiO_2 surrounding the laser ridge. Table 2 provides a summary of the relevant laser dimensions, which were used for the simulations presented in this thesis. After the epitaxial layers are grown, the laser is etched and metallized.

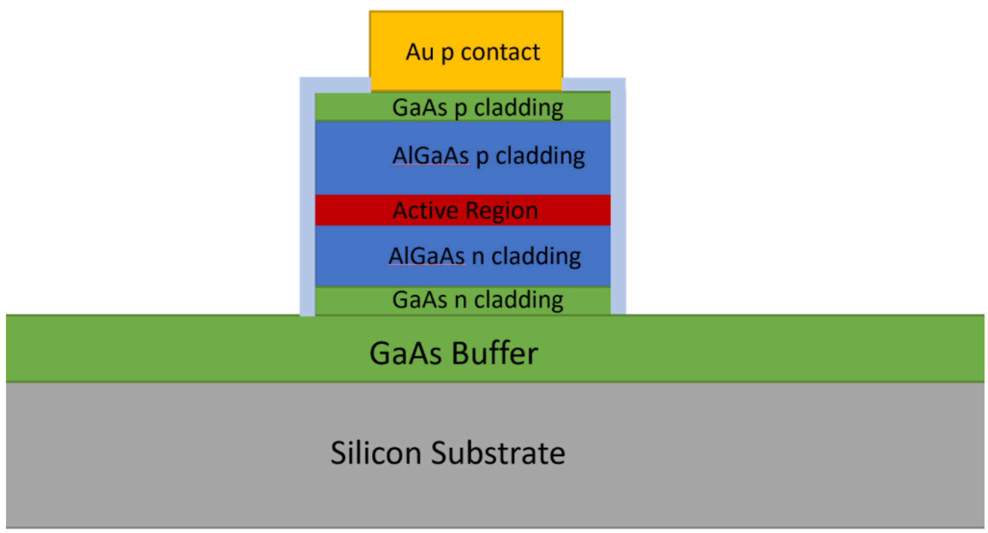

Figure 2. Quantum dot laser schematic

Laser Parameter	*Value (μm)*
Active region height	.285
AlGaAs p and n cladding height	1.4
Gold p contact height	1.0
GaAs Buffer Height	3.5
GaAs n and p cladding height	0.3
Silicon Substrate Height	200
Mesa Ridge Width	2.0 and 3.0
SiO_2 thickness	0.2

Table 2. Laser dimensions

E. Quantum Dot Laser Design for Packing with Heat Spreader

As shown in Figure 2, our typical laser design consists of a simple laser ridge. This design is insufficient for this project because we need to flip-chip bond this laser onto a heat spreader. Our flip chip bonding process requires an additional dedicated bonding surface for the n and p contacts. Therefore, during the mesa etch step of the laser fabrication process we leave two long mesa surfaces to the right and the left of the laser ridge. Figure 3 shows a schematic of this laser. These mesas on either side of the laser are the n-mesa and p-mesa contacts that will be soldered onto the corresponding n and p contacts on the heat spreader. The distance between the n contact and the laser is 50 microns, and the distance in between the laser and the p contact is 8 microns. We chose this configuration because we needed the n and p contacts far enough apart so that they do not form a short during the soldering process. Mask and processing specifications are described in Chapter III.

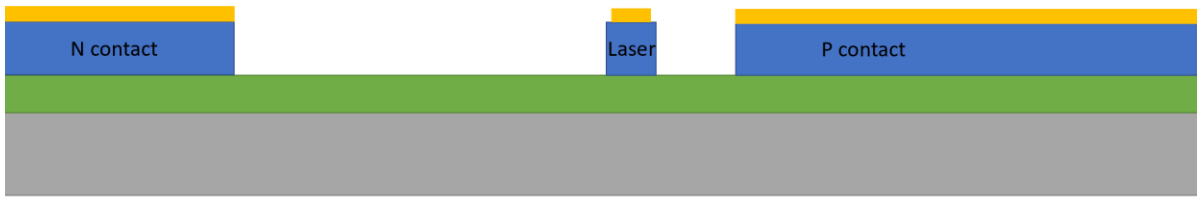

Figure 3. Simplified schematic of laser for flip chip bonding

II. Heat Spreader Design

We designed our heat spreader dimensions and metallization to be identical to the carrier wafers that fit in our ageing racks. Figure 4 shows a schematic of the carrier wafer with dimensions. Using this design, we can place the packaged laser directly into an ageing rack to evaluate its lifetime.

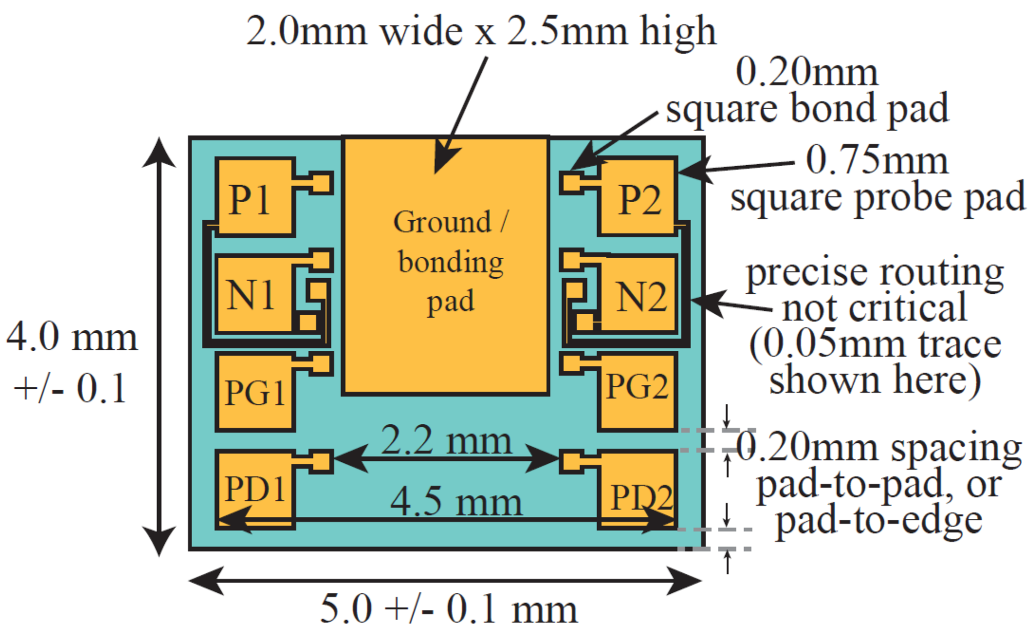

f

Figure 4. Ageing rack carrier wafer schematic with dimensions

Figure 5 shows our heat spreader design. The figure lists the dimensions and materials for the probe pads and solder. In the very center of the heat spreader (labeled B), there is a 50µm gap separating the n and p contacts. The gap is sufficiently wide to prevent solder squeezing out from both sides and coming together, creating a short. In our design, the n contact is to the left of the gap, and the p contact to the right of the gap. On the far right and left sides of the heat spreader, there are four square shaped pads, which are the n and p contacts for the ageing rack (see Figure 4). Once the laser is soldered onto the heat spreader, wirebonds will extend from the n or p probe pad where the laser is soldered to the appropriate ageing rack probe pad. Additonally, to the left of feature B there are 18 boxes next to the n solder pad. These boxes are used to align the laser to the heat spreader during the flip chip bonding process. There are corresponding notches on the laser mask which allow us to easily measure the length of the laser and determine how much of the laser we want to overhang from the heat spreader. The boxes are slightly offset from each other to allow for different alignment options. Finally, we left plenty of space behind the laser to add thermisters and additional packaging components.

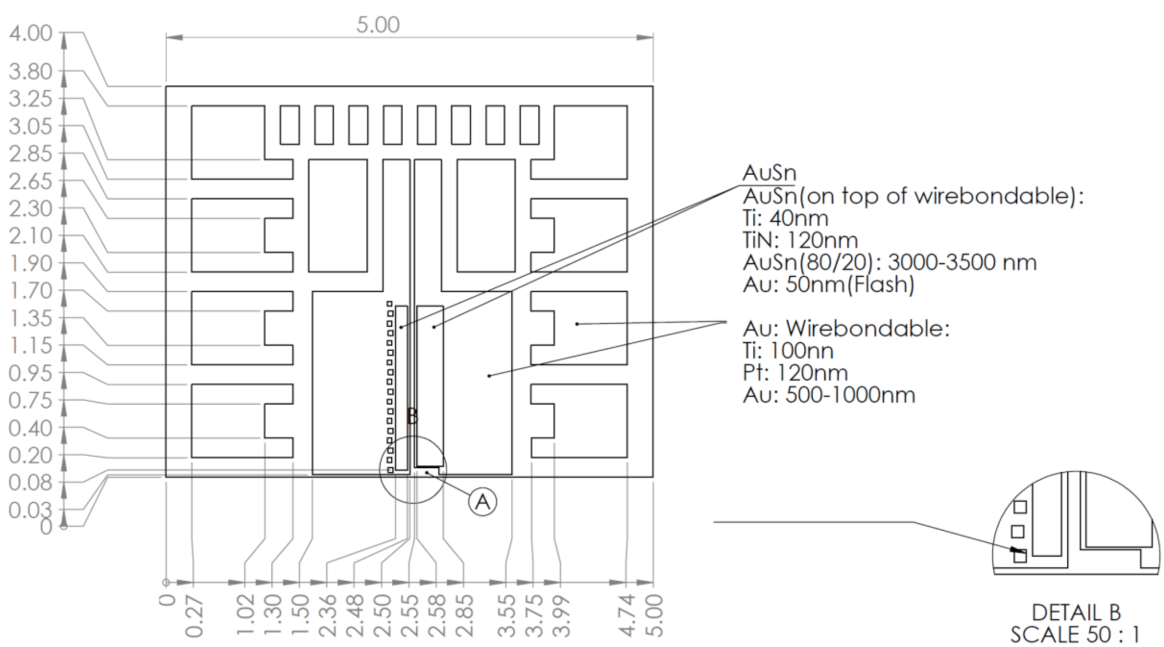

Figure 5. Heat Spreader Design. Figure designed by Dave Kinghorn

Figure 6 shows a visualization of what the laser will look like bonded ot the heat sink (not to scale). Figures 10 and 11 show a scale model of the laser bonded onto a heat sink.

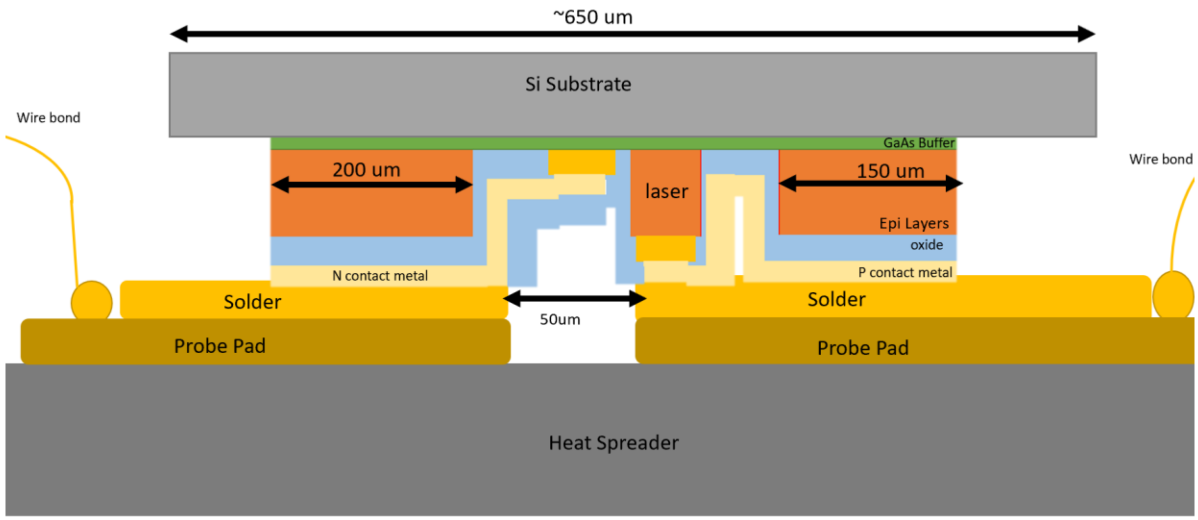

Figure 6. Laser Bonded to heat sink not to scale.

III. Laser Fabrication

This chapter will describe the laser mask and laser processing steps in more detail.

A. Step 1: Mesa Etch

The first step for processing the epi layers into a laser device is to etch the mesas using a hard etch. SiO_2 is deposited on top of the epitaxial layers. Next, a layer of photoresist is deposited, then light is shined through a photolithography mask. The photoresist softens in the areas exposed to light. The exposed SiO_2 is then etched away, and the rest of the photoresist is removed. Now, a hard etch removes the exposed epitaxial layers forming the n contact, laser, and p contact mesas. Finally, the excess SiO_2 is etched away (Figure 7).

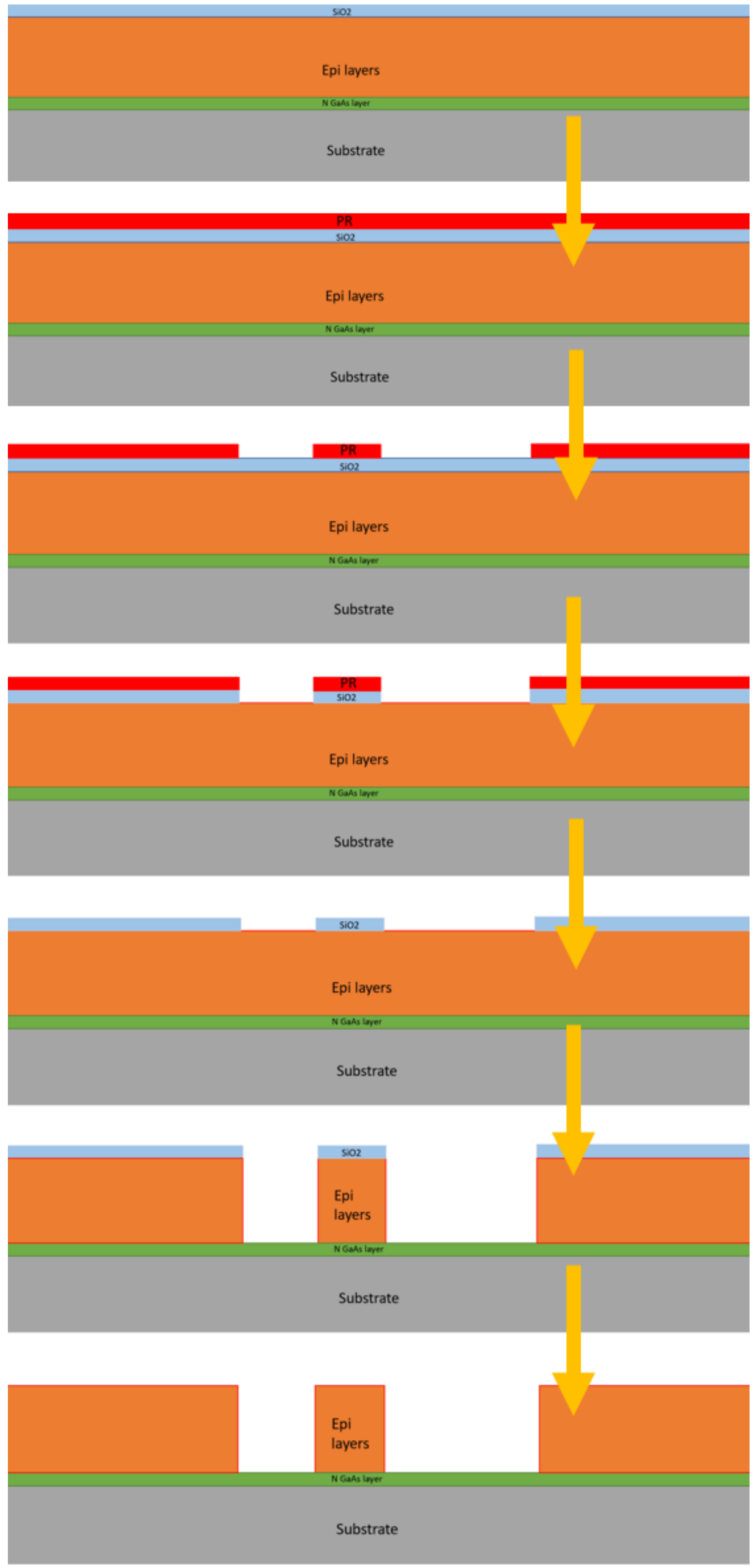

Figure 7. Mesa hard etch steps (yellow arrow indicates the process flow)

To accomplish the mesa etch step, we designed a mask with the appropriate geometry. Figure 8 shows a portion of the mesa mask in turquoise. The mesas extend 7.25mm in length. There are twelve devices on this mask. Six devices have a 2µm ridge width and six devices have a 3µm ridge width. Additionally, for every ridge width, we designed devices with three different laser to n-contact gaps: 50µm, 100µm, and 200µm in case the 50µm gap was not sufficient to prevent electrical shorts.

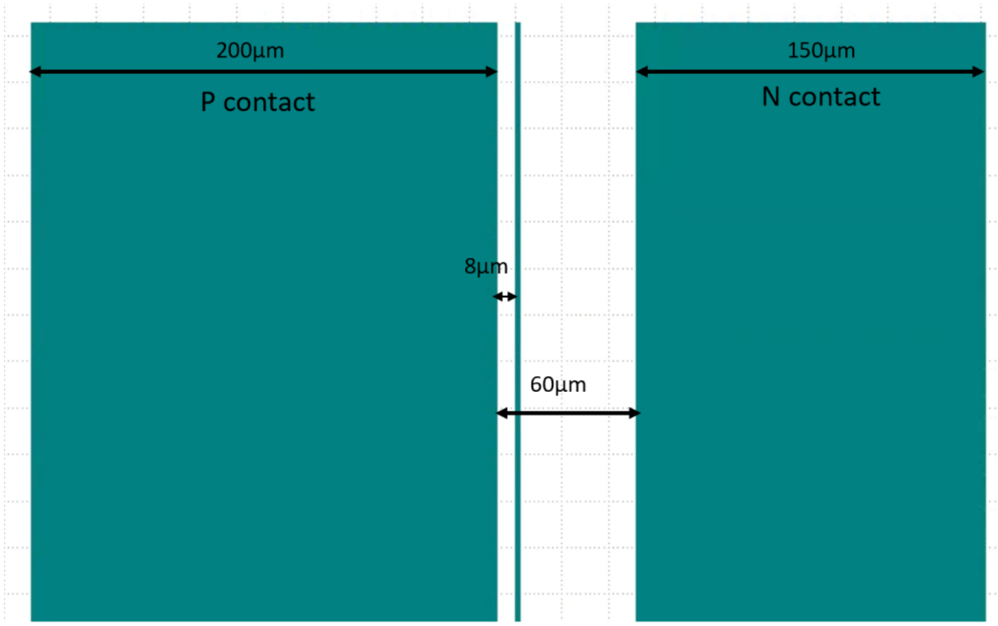

Figure 8. Mesa mask and dimensions. Center mesa is the 2µm laser ridge

B. Step 2: N-Metal Deposition

First, photoresist is deposited to completely cover the mesas. Next, light is shined through the n-metal photolithography mask, and the exposed photoresist softens and is removed. The n-metal is deposited, then a lift off process removes the excess n-metal and photoresist (Figure 9).

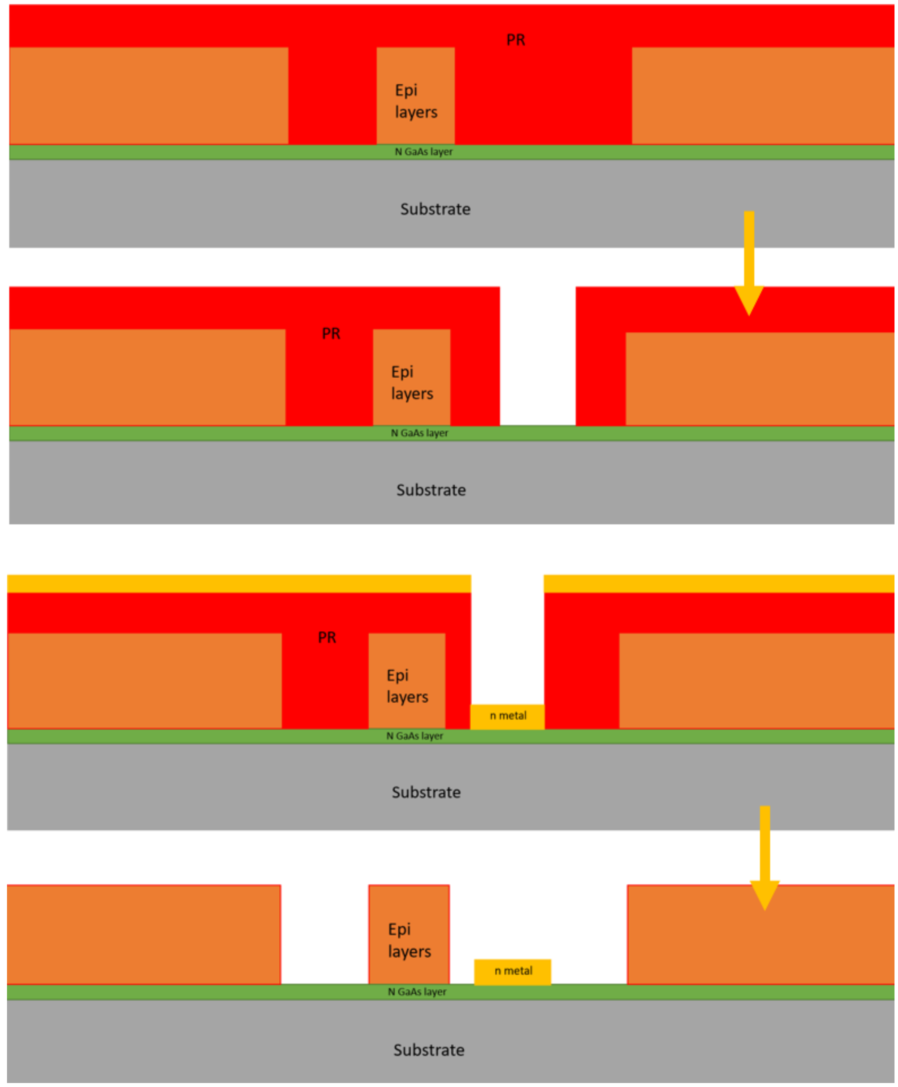

Figure 9. n-metal deposition steps (yellow arrow indicates the process flow)

Figure 10 shows the n-metal layer in azure blue, and the mesa layer in turquoise. The n-metal is 3µm to the right of the laser ridge and is 25µm wide. Additionally, the text to the left of the n-contact mesa is used to identify the device and its ridge width.

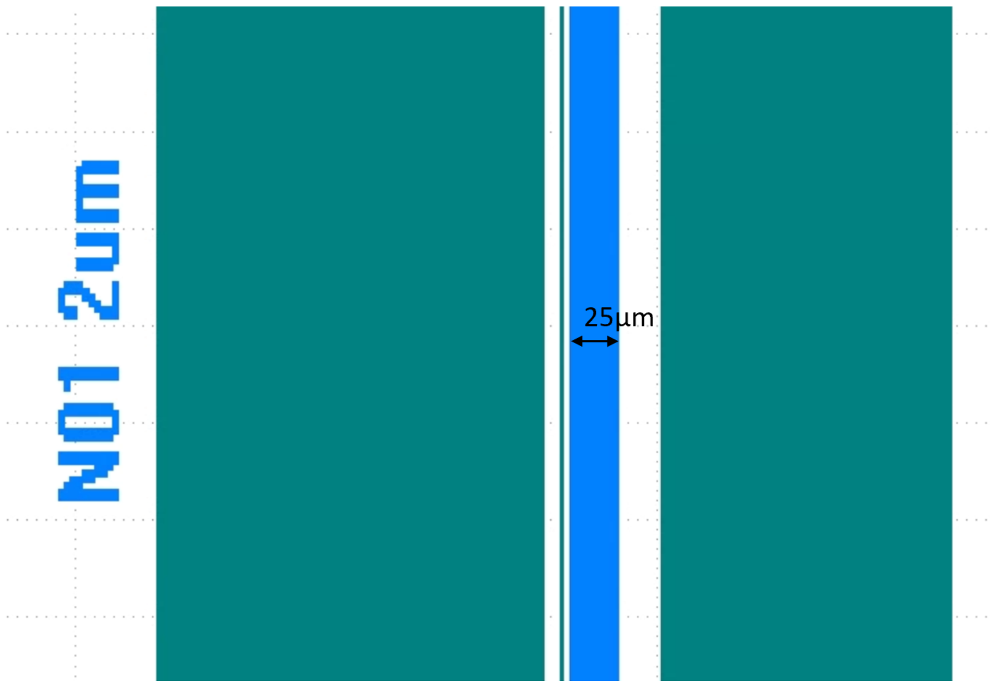

Figure 10. Mesa and n-metal mask and dimensions.

C. Step 3: P-Metal Deposition

Photoresist is deposited to completely cover the mesas. Next, light is shined through the p-metal photolithography mask, and the exposed photoresist softens and is removed. The p-metal is deposited, then a lift off process removes the excess p-metal and photoresist (Figure 11). The p-metal is centered on the mesa ridge and is 1.4µm wide for the 2µm ridge and 2.4µm wide for the 3µm ridge.

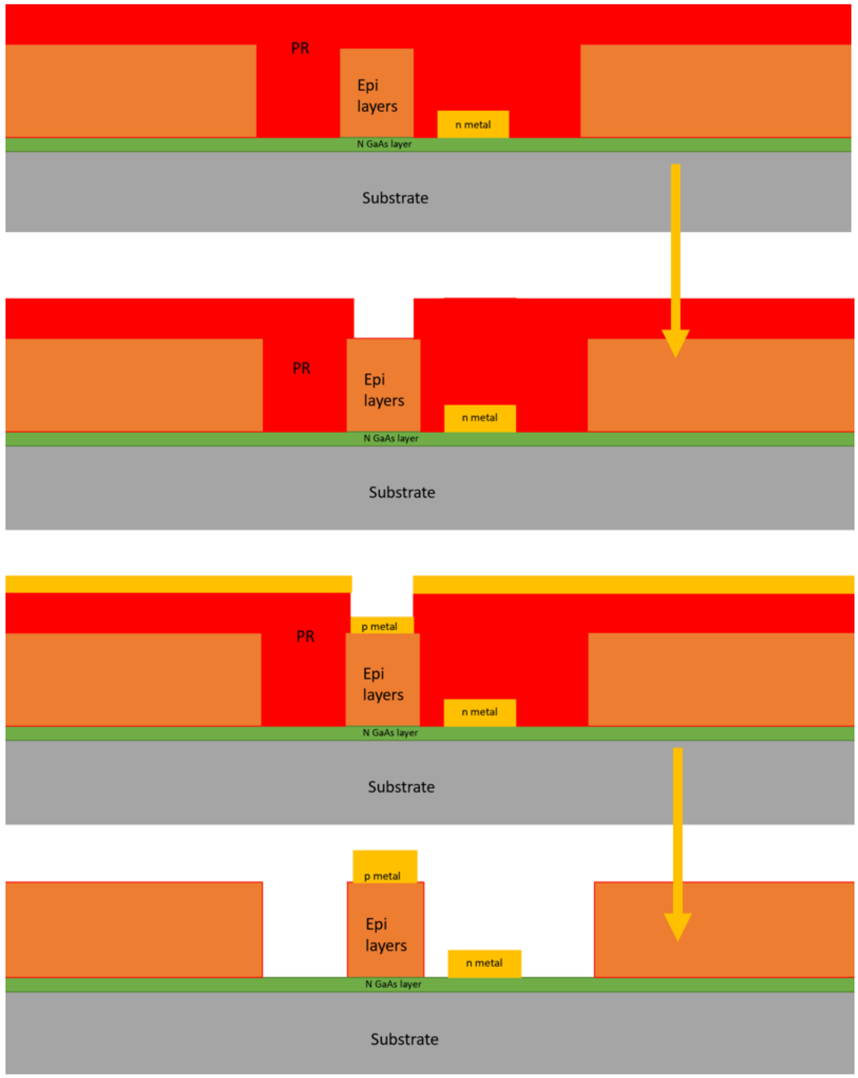

Figure 11. p-metal deposition steps (yellow arrow indicates the process flow)

D. Step 4: N and P Vias

This step protects the laser mesa from the probe metal with a layer of oxide. First, oxide is deposited over all the devices. Then, photoresist is deposited to cover all devices. Next, light is shined through the p and n via photolithography mask. The photoresist exposed to light softens and is removed. The removed portions of the photoresist expose oxide, which is then etched off. Finally, the excess photoresist is removed (Figure 12). The p via is centered on the laser ridge and is 1.1μm wide for the 2μm laser ridge and is 2.1μm wide for the 3μm laser ridge. The n-via is 14μm wide for both laser widths and is located on top of the n-metal as shown in Figure 13.

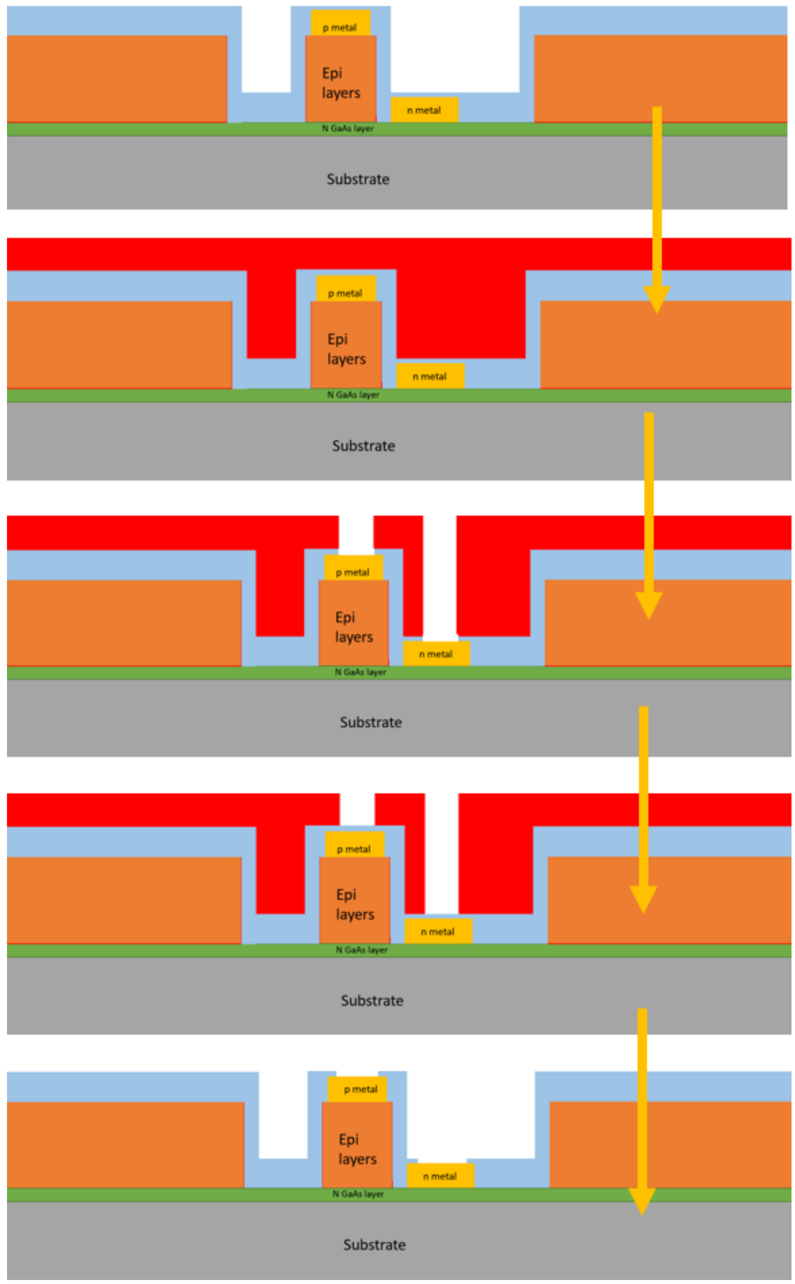

Figure 12. N and p via steps (yellow arrow indicates the process flow)

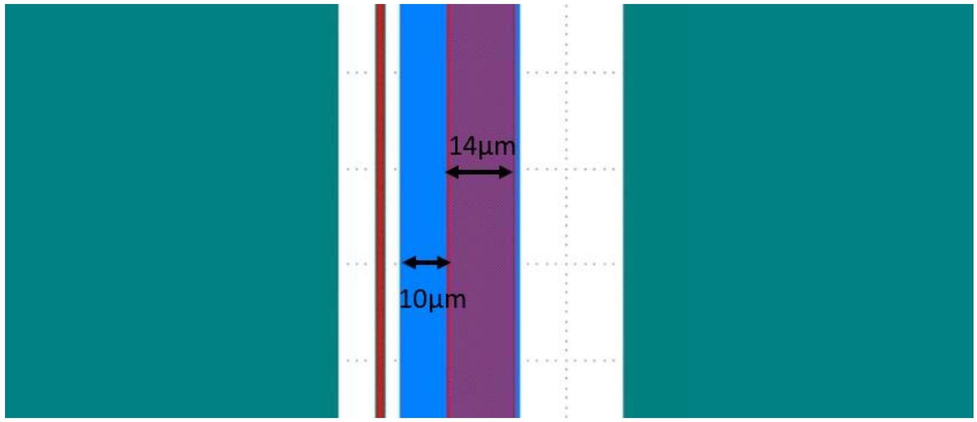

Figure 13. Three mask layers are shown: mesa layer is turquoise, n metal is azure blue, and n and p vias are red

E. Step 5: Probe Metal Deposition

Photoresist is deposited to completely cover the devices. Next, light is shined through the probe metal photolithography mask, and the exposed photoresist softens and is removed. The probe metal is deposited, then a lift off process removes the excess probe metal and photoresist (Figure 14). Figure 15 shows a portion of the probe metal photolithography mask. The probe metal layer is orange and is shown over the turquoise mesa layer with relevant dimensions. The 50 µm by 50µm squares are used to align the laser to the heat spreader during the flip chip bonding process; they also provide a simple way to measure the length of the device.

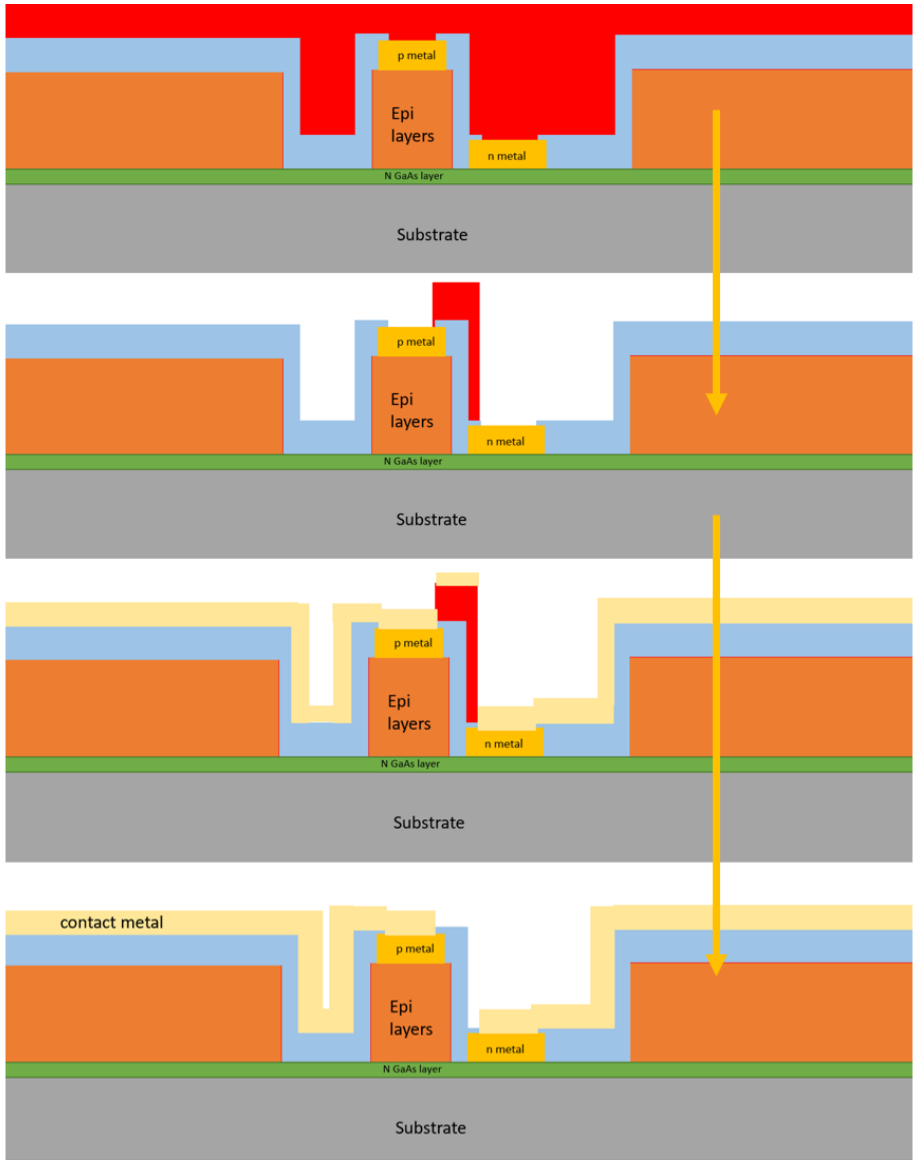

Figure 14. Probe metal deposition steps (yellow arrow indicates the process flow)

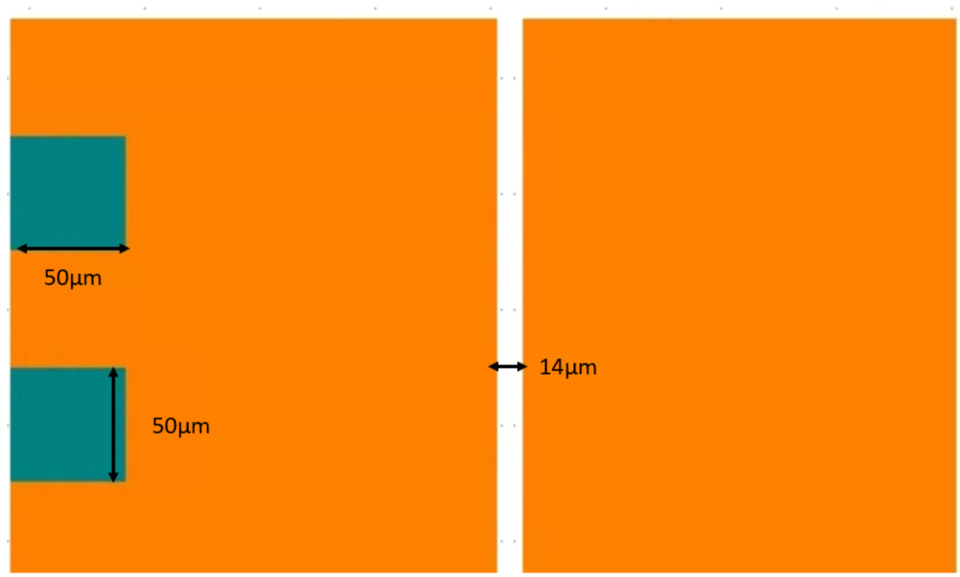

Figure 15. Two mask layers are shown: the mesa layer is turquoise and the probe metal is orange

F. Step 6: Laser to N-Contact Oxide Deposition

The sixth and final step is to deposit oxide between the laser ridge mesa and the n contact mesa. This step prevents the p-contact solder on heat spreader from the squeezing out and contacting the n-probe metal, causing a short during the bonding process. To complete this step, oxide is deposited over all the devices. Then, photoresist is deposited to cover all devices. Next, light is shined through the photolithography mask. The photoresist exposed to light softens and is removed. The removed portions of the photoresist expose oxide, which is then etched off. Finally, the excess photoresist is removed (Figure 16). The remaining oxide covers the gap between the laser ridge and the n contact mesa. Figure 17 shows a portion of the mask, with laser ridge to n-contact gap oxide layer and the mesa layers visible. The width of the laser ridge to n contact gap oxide is 50µm, 100µm, or 200µm depending on the device.

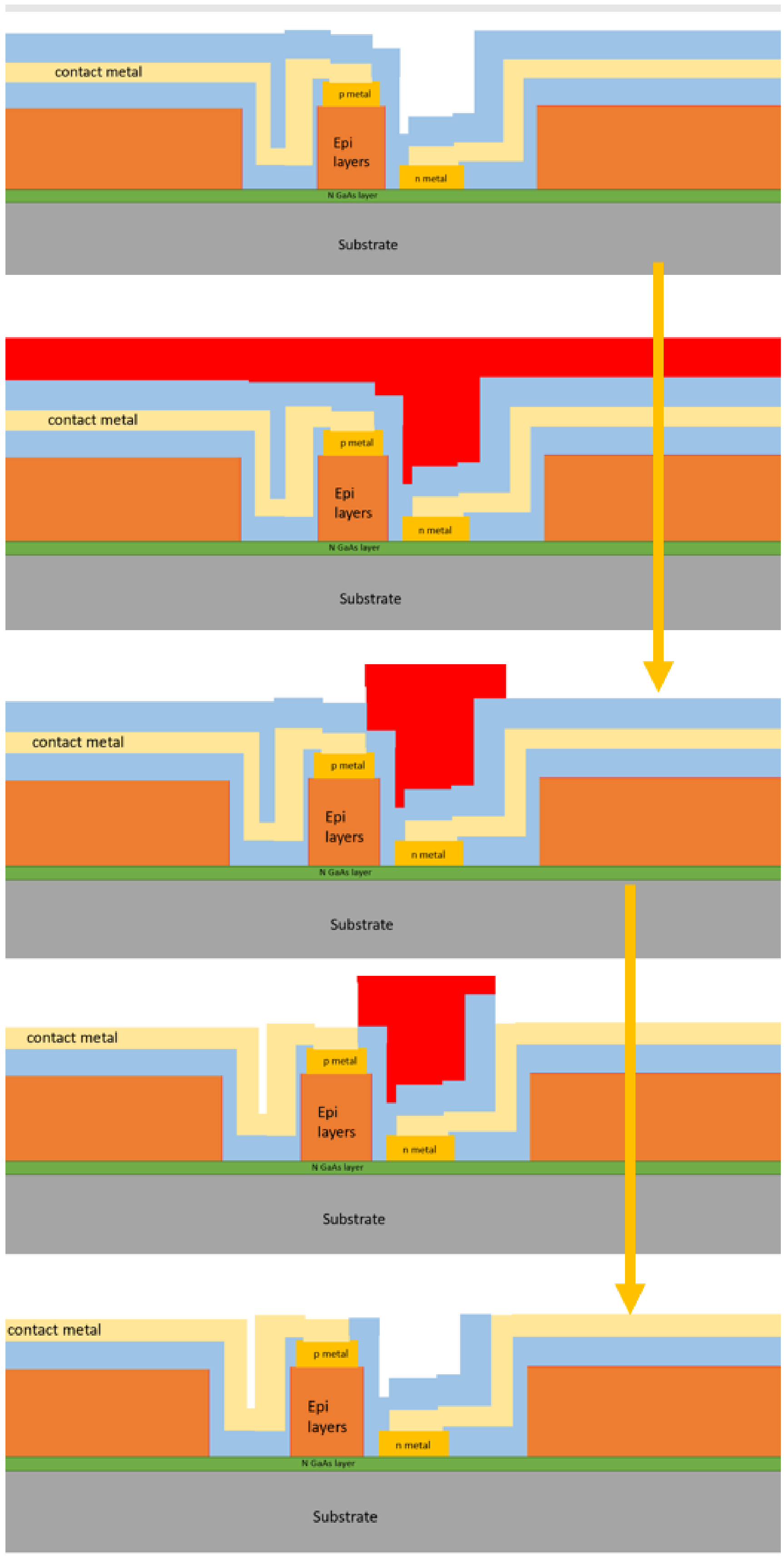
contact metal
p metal
Epi layers
n metal
N GaAs layer
Substrate
contact metal
p metal
Epi layers
n metal
N GaAs layer
Substrate
contact metal
p metal
Epi layers
n metal
N GaAs layer
Substrate
contact metal
p metal
Epi layers
n metal
N GaAs layer
Substrate
contact metal
p metal
Epi layers
n metal
N GaAs layer
Substrate

Figure 16. Laser to n-contact oxide deposition (yellow arrow indicates the process flow)

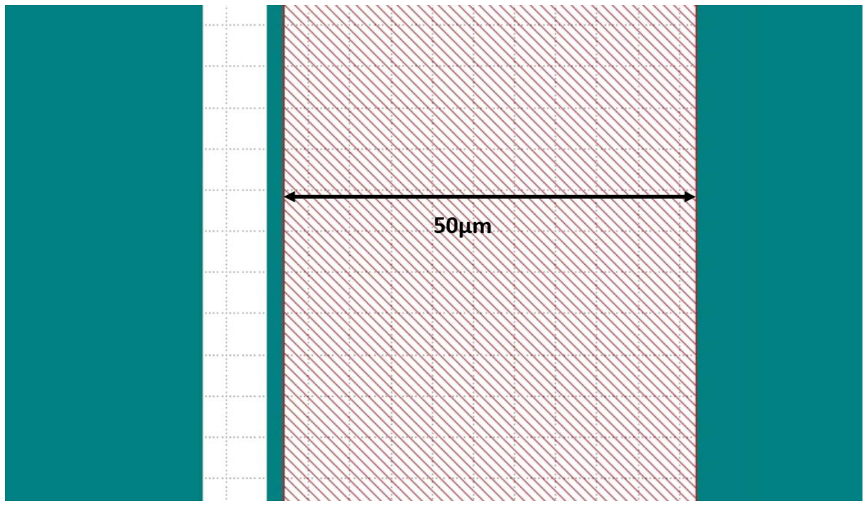

Figure 17. Two mask layers are shown: the mesa layer is turquoise and the laser to n-contact oxide layer is shaded with diagonal red lines

III. Simulations

All simulations were done using the heat transfer module in COMSOL. COMSOL is a multiphysics finite element simulation software. The heat transfer module allowed us to calculate the thermal impedance of the laser with and without a heat spreader. We started with a COMSOL simulation of the ridge laser described in Section D of the introduction with no packaging. First, we defined the geometry of the laser and then the materials. Figure 18 shows the laser ridge modeled to scale in COMSOL.

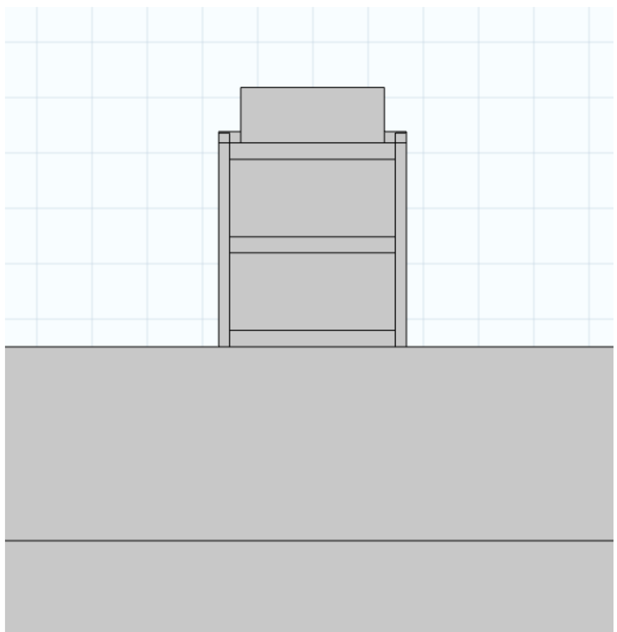

Figure 18. 3μm Laser ridge made to scale in COMSOL

We chose the silicon substrate width to be very long compared to the laser width, 1000 microns and <10 microns, respectively. This way, the silicon substrate width did not substantially contribute to the calculated thermal impedance of the laser. Next, we made a mesh and set boundary conditions. For boundary conditions, the bottom face of the silicon was set to 293K to model a TEC heat sink set to the same temperature. Additionally, the active region was set as a heat source with 0.5 W of dissipated power. The length of the laser was set to 500 microns. We calculated the thermal impedance of the laser by taking the difference between the calculated active region temperature and the heat sink temperature of 293K and then dividing that number by the heat dissipated in the active region, 0.5W. Figure 19 shows the laser ridge temperature simulation for a 2µm wide ridge laser. The simulated active region temperature is 341.7K, which results in a thermal impedance of 97.4 ºC/W for this laser. We also calculated the thermal impedance for multiple ridge widths, as shown in Figure 20.

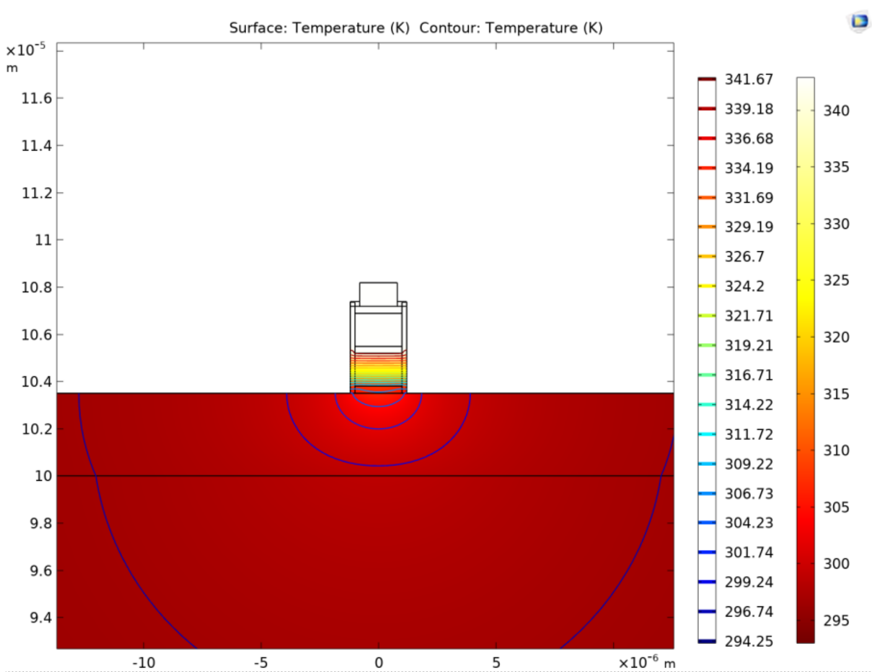

Figure 19. Simualtion of temperaure for 2 micron ridge laser

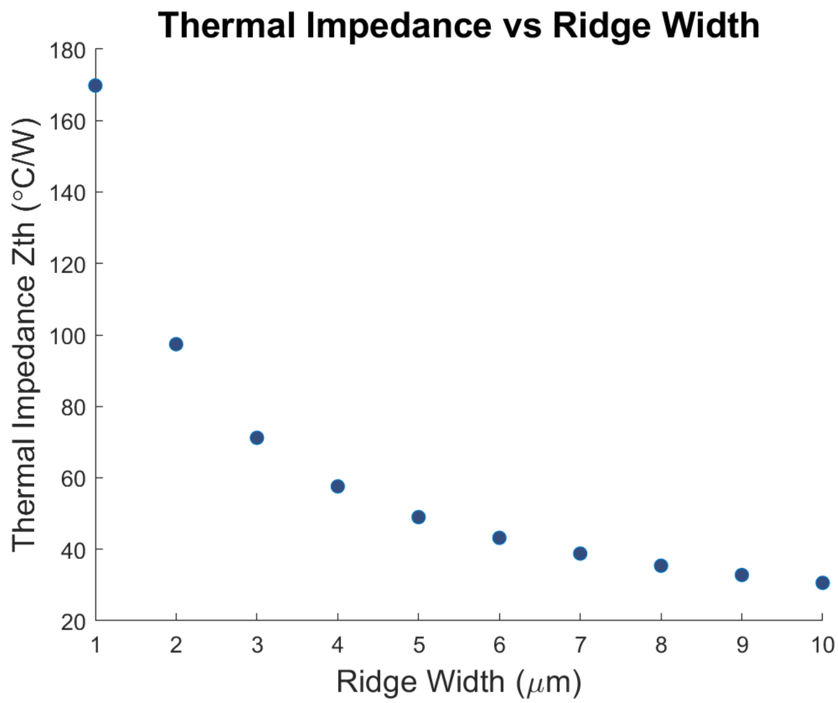

Figure 20. Thermal Impedance vs. Ridge Width for QD laser without a heat spreader

Next, we simulated the thermal impedance of the packaged laser bonded to a heat spreader. Like before, we first defined the geometry. Figure 21 and Figure 22 show two views of the laser bonded onto the heat sink. Both are modeled after the laser and heat spreader's dimensions described in Figure 5 and Table 2. The 2 micron laser ridge is easily seen in the middle right side of Figure 22. Note that the laser is upside down compared to the first simulation, since it is bonded to the heat spreader. Therefore, we set the boundary conditions of 293K to the bottom of the heat spreader. Figure 23 shows the laser ridge temperature simulation for a 2 micron ridge laser bonded on a diamond heat spreader. Temperature simulations were done for both the diamond and AlN heat spreaders and for, multiple ridge widths as shown in Figures 24 and 25, respectively. Finally, Figure 26 shows the thermal impedances of each simulation for comparison.

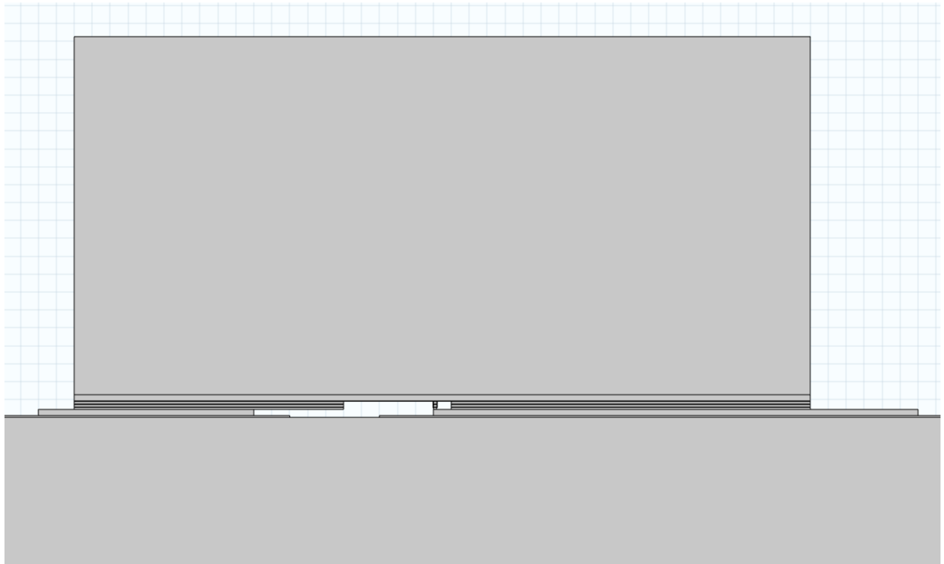

Figure 21. Zoomed out view of Laser bonded to Heat Spreader

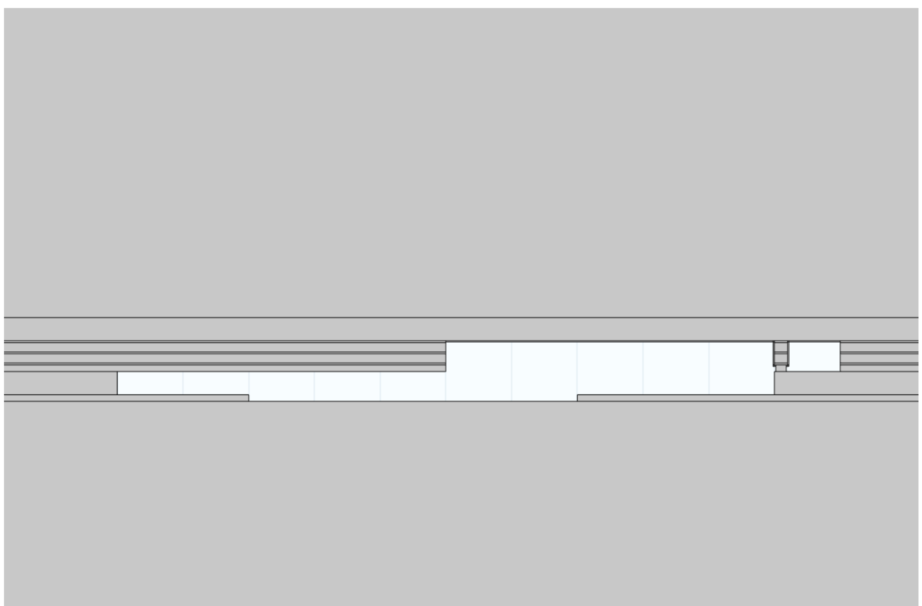

Figure 22. Zoomed in view of Laser bonded to Heat Spreader

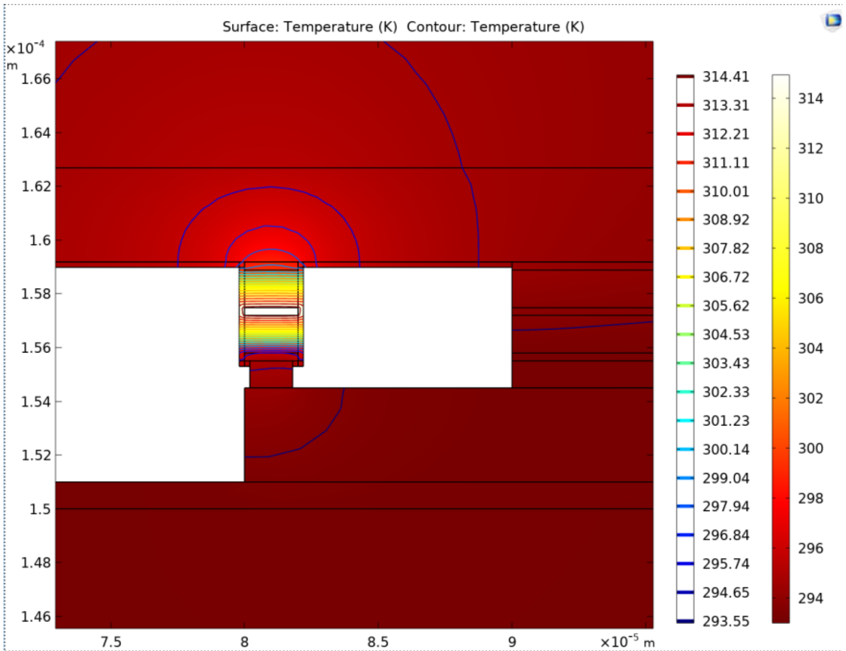

Figure 23. Simulation of temperaure for 2 µm ridge laser bonded to a diamond heat spreader

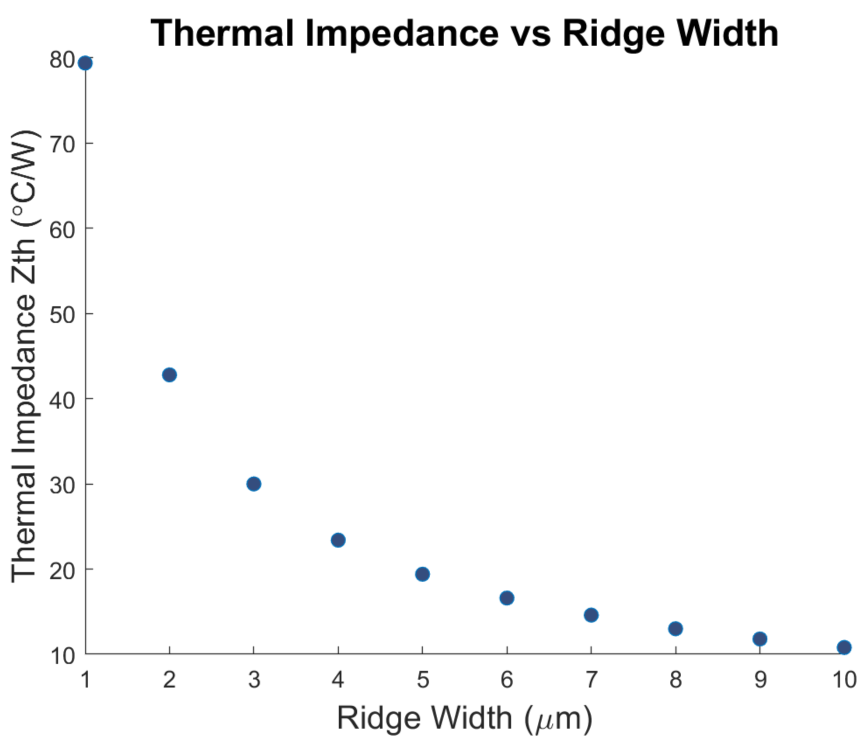

Figure 24. Z_{th} vs. Ridge Width for lasers bonded to Diamond Heat Spreader

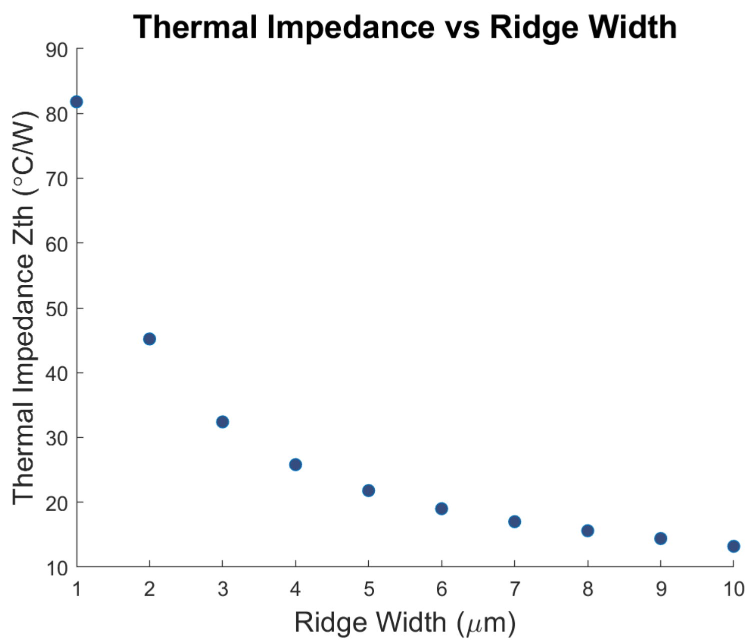

Figure 25. Z_{th} vs. Ridge Width for lasers bonded to AlN Heat Spreader

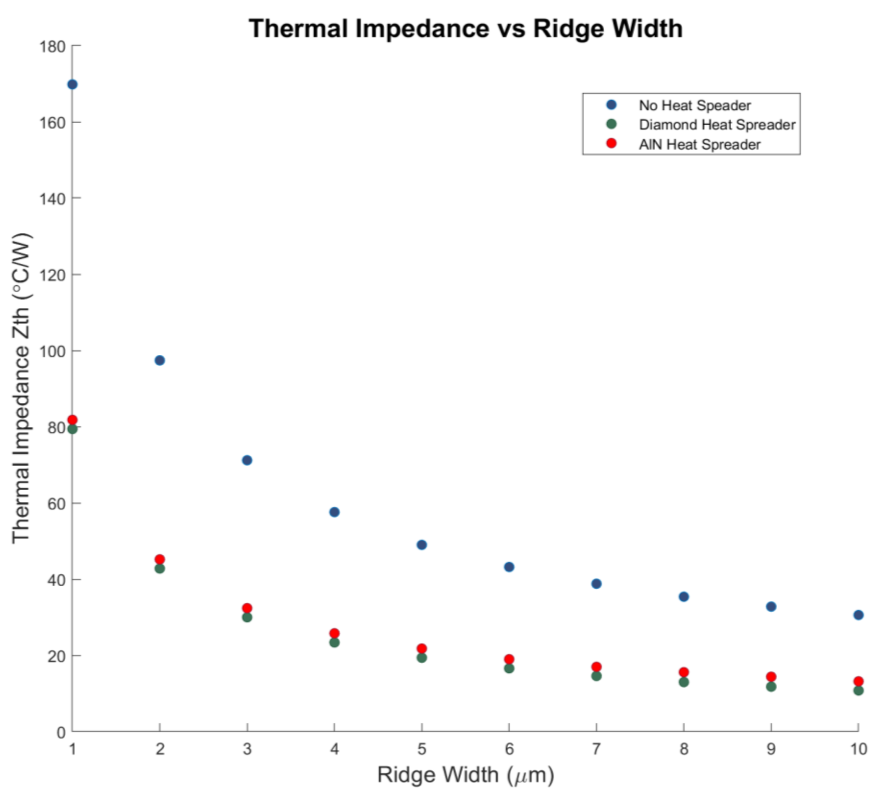

Figure 26. Z_{th} vs. Ridge Width for each packaing type

Clearly, the addition of a heat spreader produces a significant reduction to the thermal impedance. This is especially true in the case of the smaller ridge width lasers, which are most relevant for datacenter applications. For example, going from no heat spreader to a diamond heat spreader reduced the thermal impedance of a 2 micron wide ridge laser by 54.6°C/W.

Additionally, as noted in Section A of the introduction, the junction temperature can be reduced in three ways: reducing the thermal impedance, improving wall-plug efficiency, or reducing the heat sink temperature. Since we are not interested in changing the type of laser, reducing the wall-plug efficiency is not an option. However, it is worth investigating the impacts of heat sink temperature on junction temperature. Therefore, we calculated the required heat sink temperature of the non-heat spreader laser that resulted in the same junction temperature obtained from the laser with heat spreader and a heat sink temperature of 293K. We did this in COMSOL by simply reducing the heat sink temperature boundary condition on the simulation of the laser with no heat spreader until its calculated junction temperature was equal to the junction temperature of the heat spreader packaged laser with a 293K heat sink. Table 3 shows these results for a 2µm wide ridge laser.

Laser Heat Spreader	**Heat Sink Temperature (K)**	**Junction Temperature (K)**
Diamond Heat Spreader	293	314.4
AlN Heat Spreader	293	315.6
None (heat sink chosen to match diamond heat spreader junction temperature)	265.7	314.4
None (heat sink chosen to match AlN heat spreader junction temperature)	266.9	315.6

Table 3. Shows heat sink temperatures needed for desired junction temperature

As seen in Table 3, to recreate the junction temperatures realized by both heat spreader packaged lasers, the laser heat sink of the traditional laser must be below freezing. At temperatures below the dew point, condensation can form and create shorts. Therefore, for these lasers, reducing junction temperature to realize the heat spreader design's junction temperatures is not feasible. Extra steps would need to be taken to prevent any condensation from occurring (such as operating the lasers in a nitrogen environment), and the overall system efficiency would be lowered because of the higher required temperature differential across the TEC.

IV. Future Work

A. Fabricate and Cleave Lasers

The first next step is to fabricate the lasers according to the fabrication process delineated in Chapter III of this report. Once the devices are fabricated, they must be cleaved into individual laser. Tools used to handle these lasers must be small enough to handle the small width, on the order of .6mm, of the cleaved lasers.

B. Flip-Chip Bonding

Once the devices are fabricated and cleaved, they can be flip chip bonded to the diamond and ALN heat spreaders, which have already been purchased and manufactured. The laser will be flip chip bonded to the heat spreader using a Finetech flip chip bonder, with the appropriate attachments for our laser dimensions. The accuracy of the bonder is about 1um. The bonder uses an integrated side camera during the bond to ensure proper alignment without needing a translucent bond surface. The Finetech can accommodate a sample size as small as .5mm and bonding temperatures up to 400C.

C. Performance Characterization

The performance metrics we are most interested in are power output and thermal impedance. The power output can be measured by doing a simple LIV measurement. Measuring the thermal impedance is more complicated and is found by combining the results from two different measurements [11]. First, the packaged laser is placed on a TEC and set to a starting temperature (typically 20°C) and probed. Next, a constant quasi-cw current is used to operate the laser at approximately 2x threshold, with a minimal duty cycle. In this measurement, we will be adjusting stage temperature, so we use pulse operation to minimize the increase in junction temperature due to current. The optical spectrum is then recorded using an optical spectrum analyzer. Next, the TEC is adjusted in consistent increments of 0.5°C, up to the desired end temperature of 35°C. An OSA measurement is taken for each temperature step. Once these measurements are taken, the center wavelength of one Fabry Perot mode of the laser from the first measurement is chosen and is then tracked for each measurement across the temperature range. This gives us $\Delta\lambda/\Delta T$ (nm/°C). For the next measurement we run the laser under cw operation and vary the current. For each current increment we take an OSA measurement. Since we know the laser's output power and voltage for the given current from the LIV measurement, we can calculate the power dissipated in the junction for each current step. Again, we choose one FP mode in the first measurement and track it across the current/power range. This gives us $\Delta\lambda/\Delta P$ (nm/W). If we divide $\Delta\lambda/\Delta T$ by $\Delta\lambda/\Delta P$ we get the thermal impedance of the device in terms of °C/W. Once the impedance is measured experimentally, it can be compared to the simulated thermal impedance.

D. Reliability Characterization

The reliability measurement involves placing the laser package into an ageing rack and ageing it until it meets the determined failure criteria.

V. Conclusions

In conclusion, we designed diamond and AlN heat spreaders to efficiently transfer heat from an InAs quantum dot laser grown on Si to a heat sink. The simulations done demonstrate that these heat spreaders will efficiently remove excess heat and should improve many aspects of the laser's performance including increased output power, improved slope efficiency, decreased threshold current, improved wavelength stability, and extended device lifetime. We designed the laser and heat spreader masks and constructed a fabrication process for the lasers. In future work, we will manufacture the lasers, flip chip bond them to the heat spreaders, and characterize their device performance and reliability.

References

[1] A. Shehabi, S. Smith, D. Sartor, R. Brown, M. Herrlin, J. Koomey, E. Masanet, N. Horner, I. Azevedo, W. Lintner, “United States Data Center Usage Report,” Berkeley Nat. Lab., Berkeley, CA, USA, Jun. 2016.

[2] Xingsheng Liu, M. H. Hu, C. G. Caneau, R. Bhat and Chung-En Zah, “Thermal management strategies for high power semiconductor pump lasers," in *IEEE Transactions on Components and Packaging Technologies*, vol. 29, no. 2, pp. 268-276, June 2006, doi: 10.1109/TCAPT.2006.875878.

[3] Y.Horikoshi and Y. Furukawa, “Temperature sensitive threshold current of InGaAsP-InP double heterostructure lasers,” in *Japanese Journal of Applied Physics*, vol. 18, no. 4, pp. 809-815, April 1979.

[4] T. Higashi, T. Yamamoto and S. Ogita, "Temperature sensitivity of oscillation wavelength in 1.3 /spl mu/m-GaInAsP/InP quantum-well semiconductor lasers," *Conference Proceedings LEOS'96 9th Annual Meeting IEEE Lasers and Electro-Optics Society*, Boston, MA, USA, 1996, pp. 10-11 vol.1, doi: 10.1109/LEOS.1996.565096.

[5] A. Y. Liu, C. Zhang, J. Norman, A. Snyder, D. Lubyshev, J. M. Fastenau, A. W. K. Liu, A. C. Gossard and J. E. Bowers, “High performance continuous 1.3 quantum dot lasers on silicon,” Applied Physics Letters, vol. 104, no. 041104, 2014.

[6] L. Chen, E. Hall, L. Theogarajan and J. Bowers, "Photonic Switching for Data Center Applications," in *IEEE Photonics Journal*, vol. 3, no. 5, pp. 834-844, Oct. 2011, doi: 10.1109/JPHOT.2011.2166994.

[7] L. A. Coldren, S. W. Corzine and M. L. Masanovic, “A Phenomenological Approach to Diode Lasers,” in *Diode Lasers and Photonic Integrated Circuits*, 2nd ed. Hoboken, NJ, USA: John Wiley & Sons Inc., 2012, ch. 2.

[8] X. Liu, W. Zhao, L. Xiong and H. Liu, *Packaging of High Power Semiconductor Lasers*, 1st ed. pringer-Verlag New York., 2015.

[9] J. Wang *et al*., "Packaging of high power semiconductor laser arrays using a novel macro- channel cooler," *2010 11th International Conference on Electronic Packaging Technology & High Density Packaging*, Xi'an, 2010, pp. 92-97, doi: 10.1109/ICEPT.2010.5582358.

[10] M. Labudovic and M. Burka, "Heat transfer and residual stress modeling of a diamond film heat sink for high power laser diodes," in *IEEE Transactions on Components and Packaging Technologies*, vol. 26, no. 3, pp. 575-581, Sept. 2003, doi: 10.1109/TCAPT.2003.817649.

[11] T. Paoli, "A new technique for measuring the thermal impedance of junction lasers," in *IEEE Journal of Quantum Electronics*, vol. 11, no. 7, pp. 498-503, July 1975, doi: 10.1109/JQE.1975.1068661.